J. Fluid Mech. (1991), *vol.* 227, *pp.* 47–70
Printed in Great Britain

Interaction of a viscous vortex pair with a free surface

By SAMUEL OHRING AND HANS J. LUGT
David Taylor Research Center, Bethesda, MD 20084–5000, USA

(Received 11 May 1990 and in revised form 19 November 1990)

A vortex pair in a viscous, incompressible fluid rises vertically toward a deformable free surface. The mathematical description of this flow situation is a time-dependent nonlinear free-surface problem that has been solved numerically for a two-dimensional laminar flow with the aid of the Navier–Stokes equations by using boundary-fitted coordinates. For a number of selected flow parameters, results are presented on the decay of the primary vortices and their paths, the generation of surface vorticity and secondary vortices, the development and final stage of the disturbed free surface, and the influence of surface tension. High and low Froude numbers represent the two extremes of free-surface yielding and stiffness, respectively. For an intermediate Froude number, a special rebounding due to the presence of secondary vortices has been observed: the path of the primary vortex centre portrays a complete loop.

1. Introduction

In recent years the problem of a two-dimensional vortex pair (two counter-rotating vortices of equal strength) interacting with a free surface has become of interest for a number of reasons. The main attention has been focused on the study of wave signatures at a water surface caused by the vortex-induced wake of a ship (Sarpkaya & Henderson 1984; Willmarth *et al.* 1989). Another area of interest is the investigation of two-dimensional vortex and turbulence structures in which vortex pairs can develop spontaneously, travel with great speed, and can carry mass and momentum over significant distances. Here the study of the interaction of a vortex pair with a free surface would give information on the interference of the free surface with the mass and energy transport, the generation of secondary vortices, and even the creation of new vortex pairs (Couder & Basdevant 1986; Nguyen Duc & Sommeria 1988).

Barker & Crow (1977) experimented with vortex pairs near a water surface but they did not give any information on the disturbance of this surface. Experiments explicitly designed for that purpose were performed by Sarpkaya & Henderson (1984) with underwater vortices behind a hydrofoil. They observed two types of straight, sharp surface depressions which they labelled 'scars' and 'striations' according to their orientation parallel and perpendicular to the hydrofoil's movement, respectively. Vortex pairs were also produced by counter-rotating flaps (Sarpkaya, Elnitsky & Leeker 1988). This method was adopted by Willmarth *et al.* (1989) and Bernal *et al.* (1989). The latter researchers changed the free-surface characteristics through the application of surfactants.

Most of the theoretical work has been limited to potential flow. Lamb's (1932)

classical solution for two point vortices approaching a flat wall is usually used as a benchmark for the paths and speed of the vortices. The influence of a finite core of vorticity on the movement of the vortex pair was presented by Saffman (1979). Solutions for a linearized free surface were given by Wehausen & Laitone (1960) and Kochin, Kibel & Roze (1964) for a vortex near a free surface moving with a prescribed speed, whereas in Novikov's (1981) paper the vortex was free to move. A vortex pair approaching a linearized free surface was studied by Marcus (1988). Fish (1990) used a modified linearized free-surface theory to investigate the interaction of a vortex pair with ambient free-surface waves. Salvesen & von Kerczek (1976) treated the problem of a single vortex forced to move with a constant speed parallel to a nonlinear free surface. The latter nonlinear condition was imposed on the problem of a vortex pair, rising to a free surface, by Sarpkaya *et al.* (1988), Tryggvason (1988), Marcus (1988), and Telste (1989).

While the above-cited papers on potential-flow solutions give information on the surface disturbance and the paths of the vortices, viscous-flow solutions can provide insight into the decay of the vortices, the generation of surface vorticity and secondary vortices, and the final stage of the free-surface disturbances.

Peace & Riley (1983) studied the viscous-flow problem for a plane surface with either a non-slip or a perfect-slip condition. They used a viscous inner solution and an inviscid outer solution for the initial flow development. After that period, a finite-difference scheme for the Navier–Stokes equations was applied. Peace & Riley observed (for both non-slip and perfect slip) *rebounding*, that is, the vortices turning away from the free surface after their closest approach. The result for slip is limited to low Reynolds numbers according to Orlandi (1990) whose preprint came to the authors' attention during the writing of this paper. Orlandi found for a flat slip surface that rebounding diminishes with increasing Reynolds number until it ceases.

However, the assumption of a flat free surface, which was made by Peace & Riley (1983) and Orlandi (1990), does not permit the study of the generation of vorticity through the curvature of the free surface, nor can the influence of surface tension be investigated. If the free surface does not move or changes only slowly (whereas the flow field itself can be unsteady) the surface vorticity is equal to twice the curvature times the velocity tangential to the surface (Batchelor 1967). The vorticity at a flat surface is thus always zero, but this restriction does not exclude the existence of a vorticity flux at the flat free surface (which is proportional to the vorticity gradient at the surface) and the phenomenon of rebounding.

Another caveat should be mentioned with regard to the two-dimensionality of the flow model. Sarpkaya (1986) pointed out that, in reality, flow instability and vortex breakdown can occur when the vortex pair ascends; and this can occur even when the vortex pair is generated at a shallow depth as a recent study by Sarpkaya & Suthon (1990) has shown. Such a possibility must be considered in future three-dimensional flow studies.

In this paper the problem of a viscous vortex pair, approaching vertically a free surface with and without surface tension, is addressed. The flow conditions at the free surface are fully nonlinear, and hence the problems due to a curved free surface can be tackled. Preliminary results for the low Reynolds numbers of 10 and 50 without surface tension were reported by Ohring & Lugt (1989, hereinafter referred to as I). For the Reynolds number 50 these results showed qualitatively good agreement with potential-flow solutions and available experimental data.

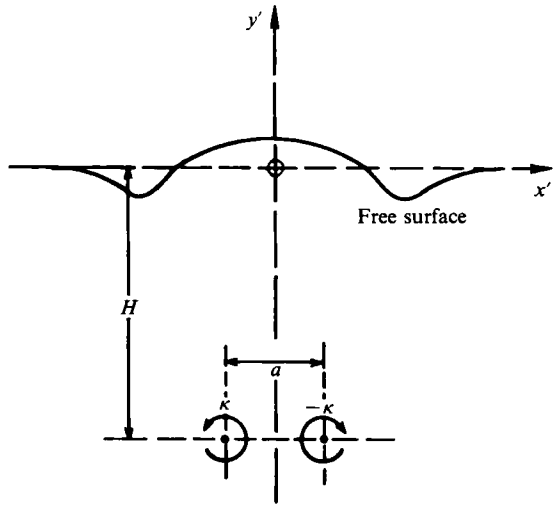

FIGURE 1. Sketch of the flow situation. The dimensional coordinates x', y' are related to the dimensionless ones by $x', y' = ax, ay$.

2. Description of the flow problem

A pair of vortices of equal strength κ but opposite sign, a distance a apart, in an incompressible Newtonian fluid vertically approaches through self-induction an initially undisturbed free surface. The flow problem is a transient one, with the fluid coming to rest after an infinitely long time. The initially undisturbed free surface is placed at $y = 0$ in a Cartesian coordinate system x, y (figure 1). The corresponding velocity components are u and v, respectively. At the initial depth H, where the vortex pair is placed, the translational velocity of the pair is V_0, which can be expressed by κ through $V_0 = \kappa/a$. The basic equations of motion are made dimensionless by the characteristic length a, the time a/V_0, and velocity V_0. The pressure is related to the dimensionless form P by $\rho V_0^2(P - y/Fr^2)$ with ρ the density of the fluid. In addition to the dimensionless depth $\delta = H/a$, the flow parameters are the Froude number Fr, the Reynolds number Re, and the Weber number We, defined by

$$Fr = \frac{V_0}{(ga)^{\frac{1}{2}}} = \frac{\kappa}{(ga^3)^{\frac{1}{2}}}, \quad Re = \frac{V_0 a}{\nu} = \frac{\kappa}{\nu}, \quad We = \frac{\sigma a}{\rho \kappa^2},$$

where ν and g are the kinematic viscosity of the fluid and the constant of gravity, respectively; σ is the coefficient of the surface tension which is considered a constant. The time-dependent, laminar flow field is then described by the initial-boundary value problem

$$u_t + (u^2)_x + (uv)_y = -P_x + \frac{1}{Re}(u_{xx} + u_{yy}), \tag{1}$$

$$v_t + (uv)_x + (v^2)_y = -P_y + \frac{1}{Re}(v_{xx} + v_{yy}), \tag{2}$$

$$u_x + v_y = 0, \tag{3}$$

with t the dimensionless time. Since the flow field is symmetric about the line $x = 0$, only the half-plane $x \geqslant 0$ with one vortex at $x = x_v$ and $y = y_v$ is considered (figure 1). The free surface is described by $y = Y(x, t)$ and is part of the solution. The remaining quadrant of infinite extent is made finite for numerical calculations by the boundaries $x = x_L$ and $y = -y_L$. Then, the boundary conditions are

$y = Y$:

$$Y_t = v - uY_x, \tag{4}$$

$$\left(P - \frac{Y}{Fr^2} - \frac{2}{Re}u_x\right)Y_x + \frac{1}{Re}(u_y + v_x) = -We\frac{Y_{xx}}{(1+Y_x^2)^{\frac{3}{2}}}Y_x, \tag{5}$$

$$\left(P - \frac{Y}{Fr^2} - \frac{2}{Re}v_y\right) + \frac{1}{Re}(u_y + v_x)\,Y_x = -We\frac{Y_{xx}}{(1+Y_x^2)^{\frac{3}{2}}}. \tag{6}$$

$y = -y_L$: $P = 0$, u, v:

obtained by second-order extrapolation along a coordinate line into the interior, (7)

$x = 0$, $-y_L < y \leqslant Y$:

$$v_x = 0, \quad u = 0, \quad P_x = 0, \tag{8}$$

$x = +x_L$, $-y_L < y \leqslant 0$: $P = 0$, u, v:

obtained by second-order extrapolation along a coordinate line into the interior. (9)

The following assumptions are made for the initial conditions at $t = 0$:

(i) The free surface is undisturbed.

(ii) A point vortex with strength κ at the position $x = x_v = \frac{1}{2}$ and $y = y_v = -\delta$ is introduced whose flow field is irrotational and is described in the quadrant $x \geqslant 0$, $y \leqslant 0$, except in the vicinity of the vortex centre, by

$$\phi + \mathrm{i}\psi = -\mathrm{i}\log\frac{(z - z_v)(z + z_v)}{(z - \bar{z}_v)(z + \bar{z}_v)}, \tag{10}$$

where $z = x + \mathrm{i}y$, $\bar{z} = x - \mathrm{i}y$, and ϕ and ψ are the potential function and the stream function, respectively, made dimensionless by κ.

(iii) The vicinity of the vortex centre with the circular boundary r_L is described by the Lamb formula for the decaying potential vortex:

$$v_\varphi = -\frac{1}{r}\left[1 - \exp\left(-\frac{r^2 Re}{4t_L}\right)\right], \quad r \leqslant r_L. \tag{11}$$

with $v_\varphi = (u^2 + v^2)^{\frac{1}{2}}$ and $r^2 = (x - x_v)^2 + (y - y_v)^2$. For a certain r_L, which is determined by the permissible error, t_L can be computed and for the examples in this paper $t_L = 0.25$. The numerical computation starts at $t = 0$.

(iv) Whereas in irrotational motion the choice of a sufficiently large initial depth δ does not affect the solution, the initial depth in a viscous fluid does. The two vortices decay and their paths are not parallel as in the inviscid-flow case but diverge slightly (Dagan 1989). However, since a decreasing δ has an effect similar to that of an increasing Re, as long as the assumption of an undisturbed surface at $t = 0$ is not violated, the value $\delta = -3$ has been chosen to keep the number of computer runs low.

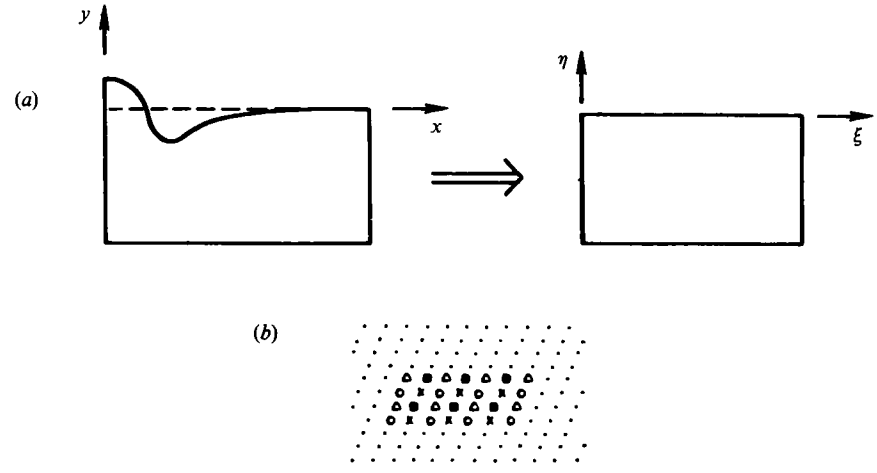

FIGURE 2 (*a*) Mapping of the physical plane (x, y) onto the computational plane (ξ, η); (*b*) the 'four-colour' scheme.

3. Outline of the numerical procedure

The numerical solution of the initial-boundary-value problem, defined by (1)–(11), is carried out with the aid of a finite-difference technique and boundary-fitted coordinates. Details are given in I, and only an outline is given in this paper. Reviews on numerical methods for free boundaries by Yeung (1982) and Floryan & Rasmussen (1989) also describe other possible methods.

For the numerical integration of this initial-boundary-value problem it is convenient to make a boundary-fitted coordinate transformation. Figure 2(*a*) is a schematic drawing of the way in which the physical plane (x, y) is mapped onto the computational domain (ξ, η). Only the coordinate lines which form the boundaries of the two regions are drawn. The coordinate lines in physical space are mapped onto a uniformly spaced Cartesian mesh with a unit mesh spacing in each coordinate direction.

As the flow field evolves in time, the grid in physical space will move and its coordinate lines will be attracted to regions of high flow gradients through the use of an adaptive-grid technique (figure 3). However, the Cartesian grid in computational space always remains fixed and uniform. This is the major advantage of using a mapping.

For all cases computed, the physical region extends from $x = 0$ to $x = 10.8$ and from $y = -6.0$ to the free surface. This physical region is mapped onto a computational space with a Cartesian grid consisting of 209 points in the ξ-coordinate direction and 201 points in the η-coordinate direction. Initially, the physical space grid contains 50 uniformly spaced grid points per unit length in the x-coordinate direction along the free surface from $x = 0$ to $x = 2.90$ with the grid then gradually stretched from $x = 2.90$ to $x = 10.8$.

The curvilinear coordinates (ξ, η) are obtained as solutions of the two elliptic partial differential equations with the physical space coordinates (x, y) as independent variables:

$$\xi_{xx} + \xi_{yy} = (\xi_x^2 + \xi_y^2) P^*(\xi, \eta), \tag{12}$$

$$\eta_{xx} + \eta_{yy} = (\eta_x^2 + \eta_y^2) Q^*(\xi, \eta). \tag{13}$$

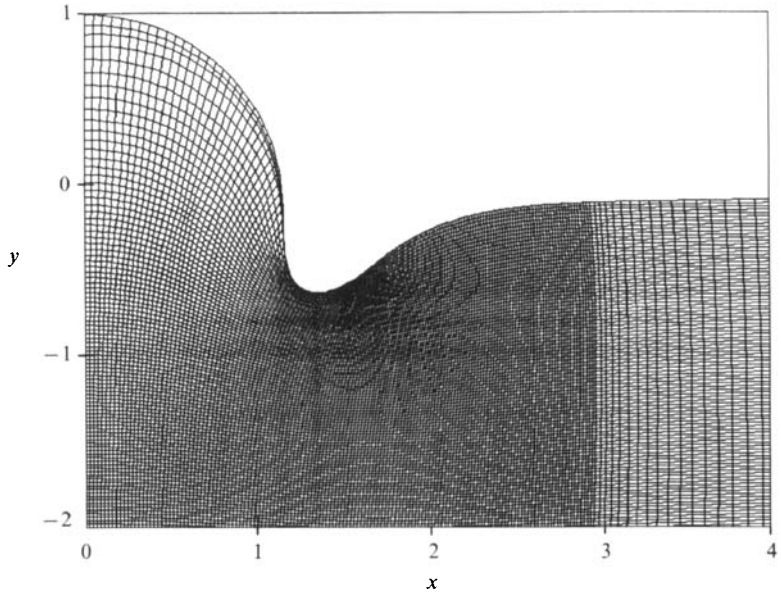

FIGURE 3. Section of the grid for $Re = 100$, $Fr = 0.8$, $We = 0$, $t = 3.475$.

P^* and Q^* are control functions described in I. Since all calculations are to be done in the rectangular computational domain, these two elliptic partial differential equations are transformed by interchanging the dependent and independent variables. As a result, the physical space coordinates (x, y) are solved in terms of the computational space coordinates (ξ, η) at each time step (Thompson & Shanks 1977).

The continuity equation (3) is replaced by an equation with pseudo-compressibility for numerically conserving mass at each physical time step:

$$P_\tau + u_x + v_y = 0. \tag{14}$$

τ is the pseudo-time. Mass conservation was excellent for all flow cases computed.

Altogether five partial differential equations, for u, v, x, y, and P, must be solved with the proper boundary conditions. The finite-difference technique for solving these equations is briefly described in the following way. All spatial derivatives, including one-sided derivatives at the boundaries, are replaced by finite-difference operators of second order in the computational space. The time-differencing procedure is implicit with a certain number of pseudo-time steps for each physical time step. The dynamic pressure field P at $t = 0$ is obtained by solving a Poisson equation for P in terms of the initial velocity field, (10) and (11). This is the only time a Poisson equation for P is used.

A 'four-colour' scheme (figure 2*b*) is used in the interior of the computational space. The use of such a scheme, which can be vectorized, resulted in an order of magnitude increase in computer speed on the Cray-XMP 24 on which the computations were performed. The four colour scheme consists of obtaining updates for P, u, v simultaneously at all the ○ points, then at all the ■ points, the × points, and the △ points, in that order. The latest available updates are used in this process.

The computational cycle for one complete pseudo-time step iteration consists of (*a*) applying the four-colour scheme to compute updates for x and y followed by obtaining the latest updates for y at successive points along the symmetry

boundary (8); (*b*) applying the four-colour scheme to compute updates for u, v, and P; (*c*) obtaining updates for P and v at successive points along the symmetry boundary (8); (*d*) obtaining updates for P, u, v, and Y at successive points along the free surface; and (*e*) obtaining updates for u and v at successive points, first along the boundary $x = x_L$ from (9) and then along the boundary $y = -y_L$ from (7).

At the completion of this computational cycle, after the latest updates for x, y, u, and v satisfy certain convergence criteria at all points, these updates are the solution at the new time level $n+1$. If the convergence criteria are not met, cycle (*a*)–(*e*) is repeated until they are met. The accuracy of the numerical scheme was checked with fine grids in I.

Computations of the stream function are not presented in this paper. Therefore, the streamline pictures show only selected streamlines obtained numerically from the velocity fields. These selected streamlines do not represent equally spaced incremental values of the mass flux.

The surface vorticity ω_s is of interest for the study of secondary vortices and is computed with the aid of $\omega = \partial v/\partial x - \partial u/\partial y$. The well-known formula for ω_s being 'twice the surface curvature times tangential surface velocity' is only valid along a streamline, that is, for a fixed free surface. The flow field itself can be unsteady. This formula is helpful in the discussion of the results in the next section because it gives good approximate data for a slowly changing free surface. Comparisons of computations with the two kinds of formulae for the surface vorticity have shown this in I.

4. Results

Numerical calculations were performed for $Re = 100$, $Fr = 0.2$, 0.4, and 0.8, without surface tension, that is, for $We = 0$. Also, for $Fr = 0.2$, surface tension was studied for $We = 10$; for $Fr = 0.4$, Weber numbers of 1 and 10 were selected. The influence of various Reynolds numbers on the flow field was investigated by computing a few cases for $Re = 10$ and 50. In these examples the Froude numbers were chosen to be $Fr = 0.356$ and 1.125 to compare the results with those obtained from experiments and for inviscid flows.

Two extreme flow situations are exemplified by the 'high' and 'low' Froude numbers. At high Froude number the free surface can easily be deformed and is not a strong barrier against the ascending vortex pair. At low Froude number, in contrast, the free surface acts like a stiff wall. Between these two cases, transitional situations occur. The intermediate case of $Re = 100$, $Fr = 0.4$ is the most interesting with respect to evolving flow patterns.

In unsteady viscous flow, the centre of the vortex can be defined either as the place of local extremal vorticity or as the centre of the whirl, that is, the centre of nested instantaneous streamlines (Lugt 1983). Whereas the vorticity field is independent of the choice of the reference frame, the streamlines are dependent on it. In all of the following figures the instantaneous streamlines are in a reference frame fixed to the undisturbed free surface and the vortex is moving relative to this frame. The centre of nested streamlines does not coincide with the location of extremal vorticity. In what follows, the phrase *vortex centre* refers to the place of local extremal vorticity. Solid equivorticity lines represent negative values, dashed lines positive values.

Figures 4 and 5 display equivorticity lines and instantaneous streamlines, at four times and at $t = 3.475$ respectively, for $Re = 100$, $Fr = 0.8$ and $We = 0$. Near the centreline $x = 0$ the vortex pair pushes the free surface up and creates nearby a local

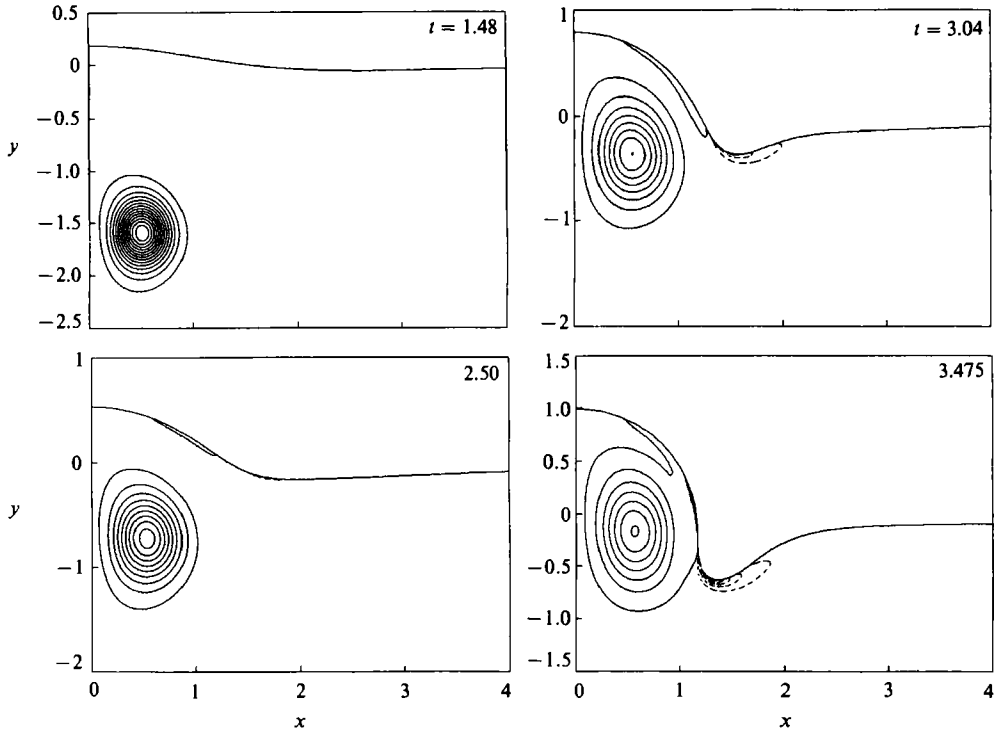

FIGURE 4. Equivorticity lines for $Re = 100$, $Fr = 0.8$, $We = 0$ at four different times. The ω-contours are ..., -3, -1, $+1$, $+3$, ...

depression, called a 'scar' by Sarpkaya & Henderson (1984). The computation is stopped at $t = 3.475$ before the surface has reached its peak for numerical reasons because the adjustable grid is no longer adequate to handle the steep free surface (figure 3). The instantaneous streamlines to the right of the scar in figure 5 ($t = 3.475$) clearly show wave motion to the right, revealed by the non-zero angle between streamlines and free surface.

It may be recalled that an approximate formula for the surface vorticity is 'twice the surface curvature times tangential surface velocity'. Applied to the present situation, the occurrence of positive vorticity at the scar can be explained by the changing sign of the surface curvature. The transport of positive vorticity into the fluid is then controlled by the vorticity flux at the surface whose magnitude is indicated in figure 4 by the narrowness of the equivorticity lines.

The path of the vortex centre is depicted in figure 6. It is straight up and conforms with those of previous cases of high Froude numbers for inviscid fluids (Sarpkaya *et al.* 1988; Marcus 1988; Telste 1989). For comparison, the classical path of a point vortex with a flat surface (Lamb 1932) is given by

$$x^2 + y^2 = 4x^2y^2, \tag{15}$$

with a unit distance between the two vortices far away from the origin of the coordinates system. (Actually, the 'unit' distance is only approximate, say about 0.99, because of the choice in §2 of the initial depth δ a finite distance away from the free surface.)

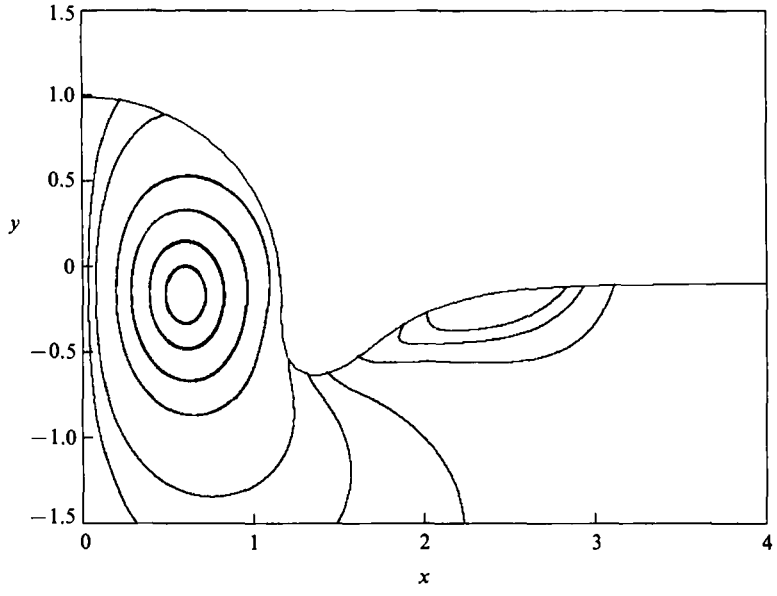

FIGURE 5. Streamlines for $Re = 100$, $Fr = 0.8$, $We = 0$ at $t = 3.475$.

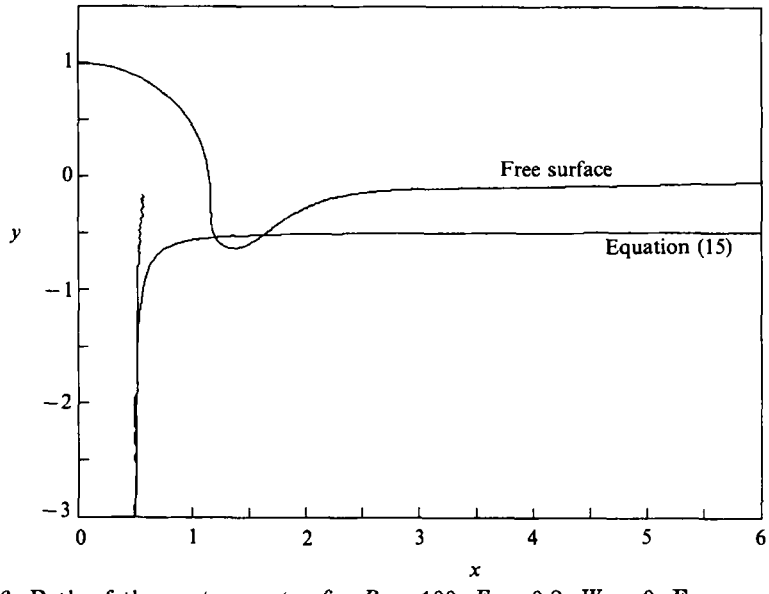

FIGURE 6. Path of the vortex centre for $Re = 100$, $Fr = 0.8$, $We = 0$. For comparison, Lamb's potential-flow solution for a flat surface, (15), is included. The free-surface is plotted for the final time $t = 3.475$.

The decrease of $|\omega_{\text{extremum}}|$ at the vortex centre with time is displayed in figure 7. From (11) it follows that the vorticity at the vortex centre is

$$\frac{|\omega_{\text{extremum}}|}{Re} = \frac{1}{2(t_{\text{L}}+t)}. \tag{16}$$

The numerical computations show that up to $t = 6$ the vorticity extremum decreases according to (16) with such an accuracy that the curves for all cases considered in this

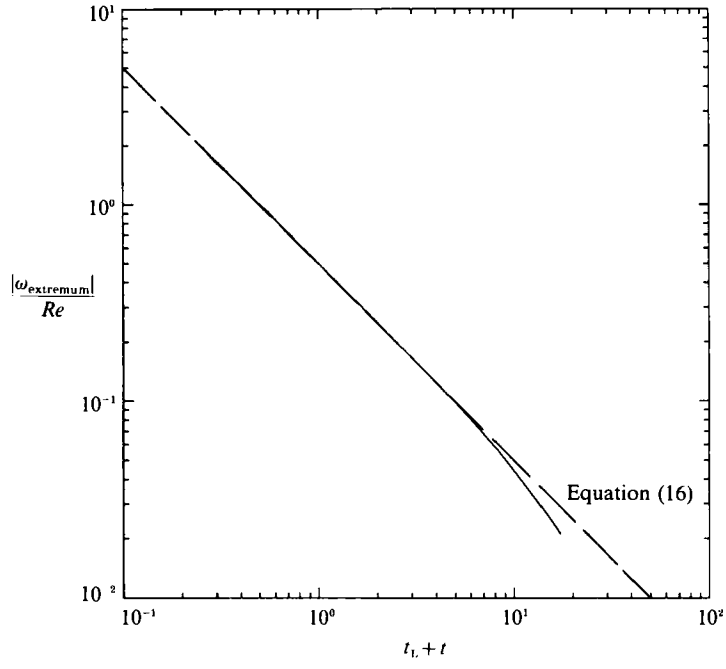

FIGURE 7. Decrease of $|\omega_{extremum}|$ with time for all cases.

paper and in I fall on the line shown in figure 7. Beyond $t = 6$, the vortices decay more rapidly.

The effect of a low Froude number on the solutions is presented for $Re = 100$, $Fr = 0.2$, $We = 0$. Equivorticity lines and streamlines are shown in figures 8 and 9. The free surface rises only slightly to form a flat mound, but quite a sharp scar is generated. The surface then comes to rest by means of damped oscillation when $t \to \infty$. To the right of the scar, positive vorticity is created (figure 8, $t = 3.52$) that in time causes secondary vortex shedding from the surface into the interior of the fluid.

The generation and shedding of a vortex behind the scar are similar to those behind solid bodies. First, a tongue of vorticity develops with closed streamlines, indicating the generation of a vortex attached to the body or the scar. This tongue is stretched by the surrounding flow or the primary vortex, with the secondary vortex still attached to the surface by a 'feeding sheet' of vorticity. The occurrence of a vorticity extremum, then signals vortex shedding from the body or the scar.

At $t = 6.52$, positive vorticity with the weak secondary vortex has been wrapped around the primary vortex which produces this effect. The secondary vortex is so weak that it does not even cause the instantaneous streamlines of the primary vortex to deviate from their circular pattern (figure 9, $t = 6.52$). At $t = 11.02$ this positive vorticity field has disappeared (at least for the level of vorticity contours plotted).

The path of the primary vortex centre lies below that of Lamb's solution (figure 10). Its form is slightly wavy because the vortex is first pushed down a little by the scar, rises, and then rebounds a tiny bit owing to diffusion.

Surface tension of the magnitude determined by $We = 10$ flattens the surface to the extent that the surface is barely deformed, and no positive vorticity is generated (figure 11). Streamlines are depicted for $t = 3.52$ only (figure 12). The path of the vortex coincides almost with that of Lamb's solution (figure 10). Rebounding does not occur.

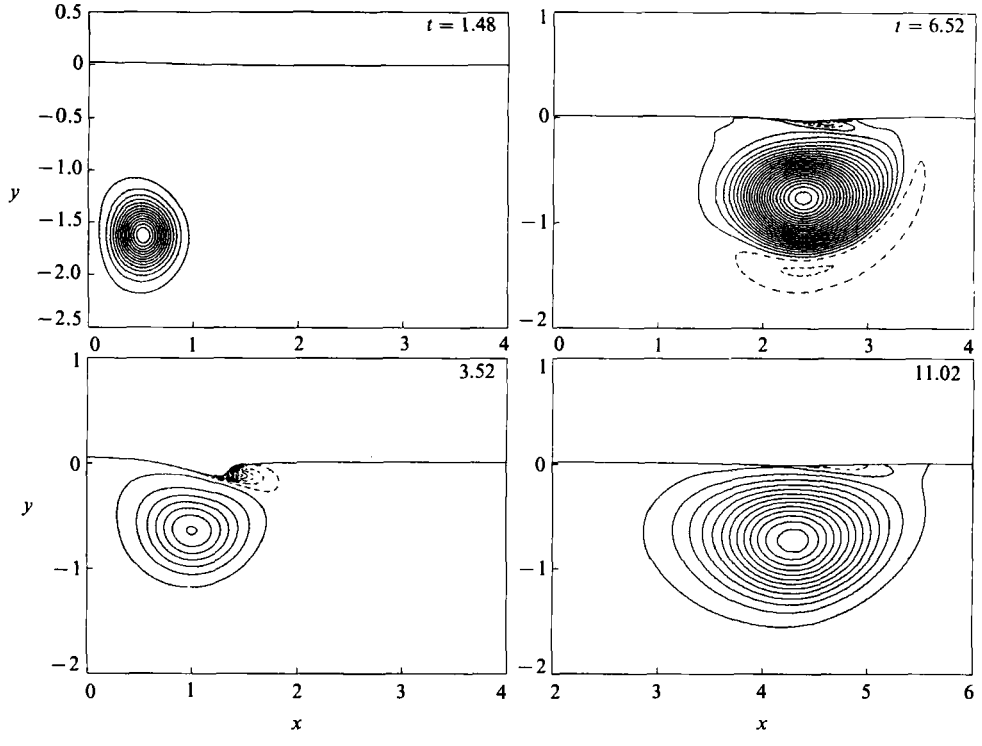

FIGURE 8. Equivorticity lines for $Re = 100$, $Fr = 0.2$, $We = 0$ at four different times. The ω-contours are ..., -3, -1, $+1$, $+3$, ..., for $t = 1.48$ and 3.52 and ..., -0.15, $+0.15$, $+0.45$, ..., for $t = 6.52$ and 11.02.

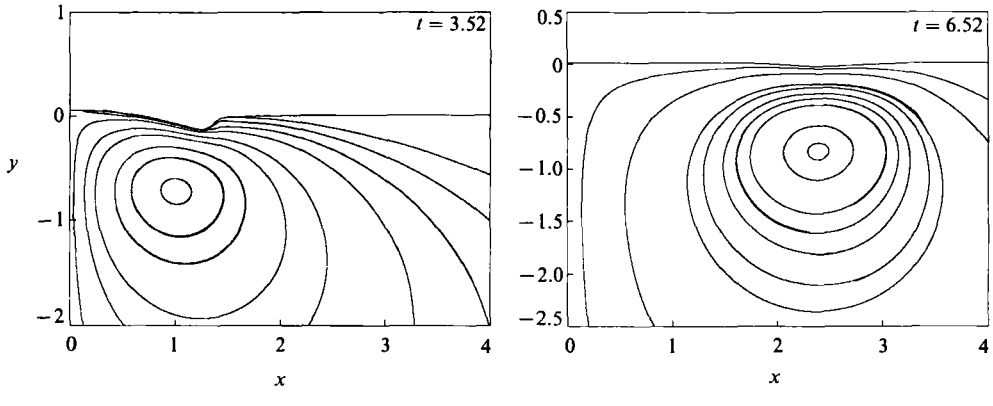

FIGURE 9. Streamlines for $Re = 100$, $Fr = 0.2$, $We = 0$ at two different times.

$Fr = 0.4$ is the most interesting case. The Weber numbers are chosen as $We = 0$, 1, and 10. Equivorticity lines and streamlines without surface tension are shown in figures 13 and 14 for eight and four different times, respectively.

As to be expected, the free surface reaches its peak between the peaks for $Fr = 0.8$ and 0.2. At the maximum elevation, the scar is deepest, associated with the generation of large positive vorticity ($t = 3.52$ in figures 13 and 14) which spreads to the right of the scar through the action of the primary vortex. A short time later the primary vortex rebounds and stretches the adjacent positive vorticity field to the

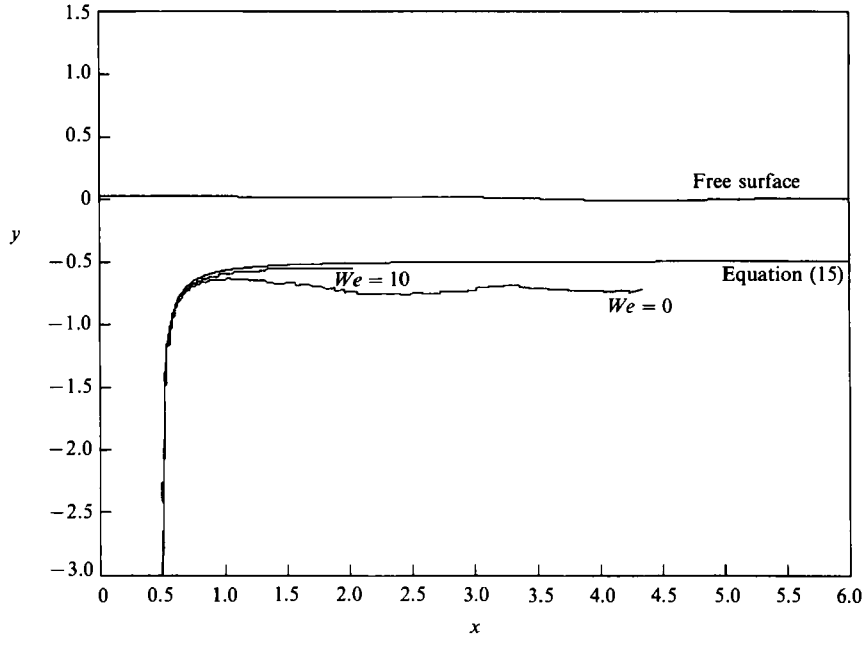

FIGURE 10. Paths of the vortex centre for $Re = 100$, $Fr = 0.2$, $We = 0$ and 10. For comparison, Lamb's potential-flow solution for a flat surface is included. The free surface is plotted for the final time $t = 11.02$.

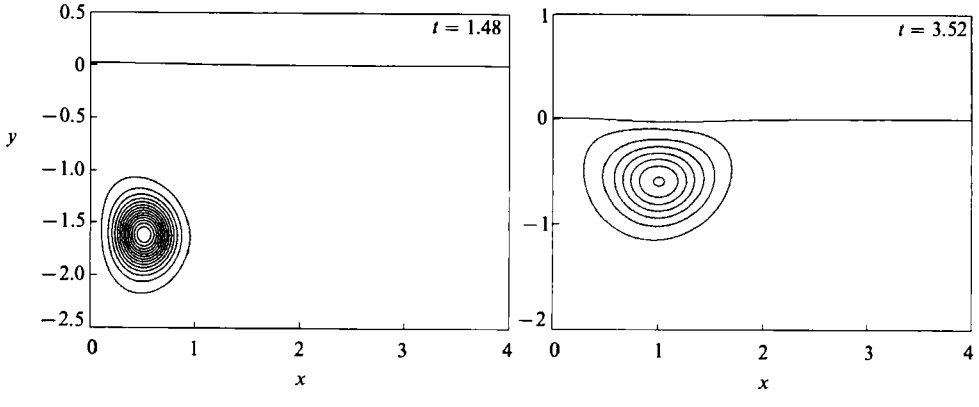

FIGURE 11. Equivorticity lines for $Re = 100$, $Fr = 0.2$, $We = 10$ at two different times. The ω-contours are ..., -3, -1.

point of vortex shedding (figure 13, $t = 4.0$). A secondary vortex, strong enough to exhibit a circular streamline pattern (figure 14), is created and shed.

Both primary and secondary vortices form a system that consists of two counter-rotating vortices with the primary vortex stronger than the secondary one. It is well-known from the kinematics of two point vortices that through mutual induction the smaller vortex rotates around the larger one which itself moves along a smaller circular path (figure 13). There is a high-speed flow between the primary and secondary vortices indicated by the crowding of streamlines between them (figure 14). During that time period the surface near the centreline displays damped

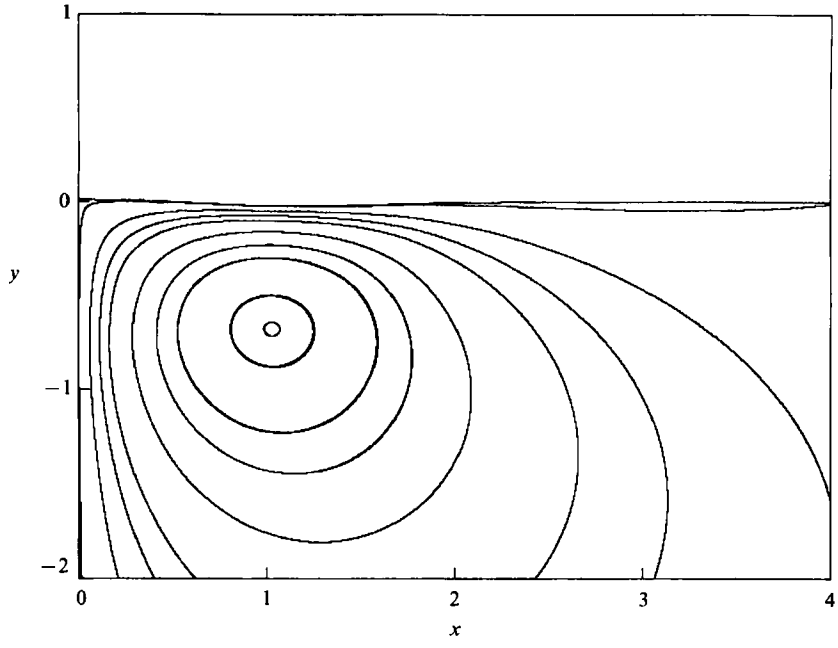

FIGURE 12. Streamlines for $Re = 100$, $Fr = 0.2$, $We = 10$ at $t = 3.52$.

oscillation. A second but flatter scar occurs; this double scar appears to be a novel feature, not observed in previous studies. Meantime, a second vortex with positive vorticity has developed near the free surface ($t = 5.02$) and is wrapping around the primary vortex ($t = 6.52$) (figure 13). This weaker positive vortex appears as wavy streamlines in figure 14 ($t = 5.02$). While the secondary vortices dwindle away, the primary vortex rises again and is then deflected to the right. The vortex disturbs the free surface, but this time only slightly because it has weakened considerably. One observes thus the phenomenon that the rebound of the primary vortex extends to a complete loop of the path (figure 15).

The observation of a complete loop is known for a vortex pair approaching a non-slip wall (Orlandi 1990). This was also found earlier by Walker *et al.* (1987) for the analogous axisymmetric problem of a vortex ring impinging on a non-slip wall. The explanation goes back to Harvey & Perry (1971). The approaching vortex pair or vortex ring induces vorticity of opposite sign along the non-slip wall. This vorticity is then sucked by the vortex into the fluid, a process that causes flow separation and subsequently the generation of a secondary vortex.

Looping of a vortex pair has not yet been observed for a flat slip surface, either in numerical computations or in experiments (with almost flat surfaces). However, looping was detected by Bernal *et al.* (1989) for vortex rings which approached a slip surface contaminated by surfactants. These surfactants slow down the fluid motion along the free surface and, hence, generate vorticity in a similar fashion to that of the non-slip surface. For a vortex pair, Bernal *et al.* (1989) observed a stronger rebound with surfactants but not a loop.

It becomes clear now that the loop observed in figure 15 is due to the production of positive vorticity behind the scar that would not have occurred at a clean, flat slip surface. Thus, the high curvature of the scar as a source for positive vorticity plays the role of non-slip at a flat surface in generating the loop. This statement is

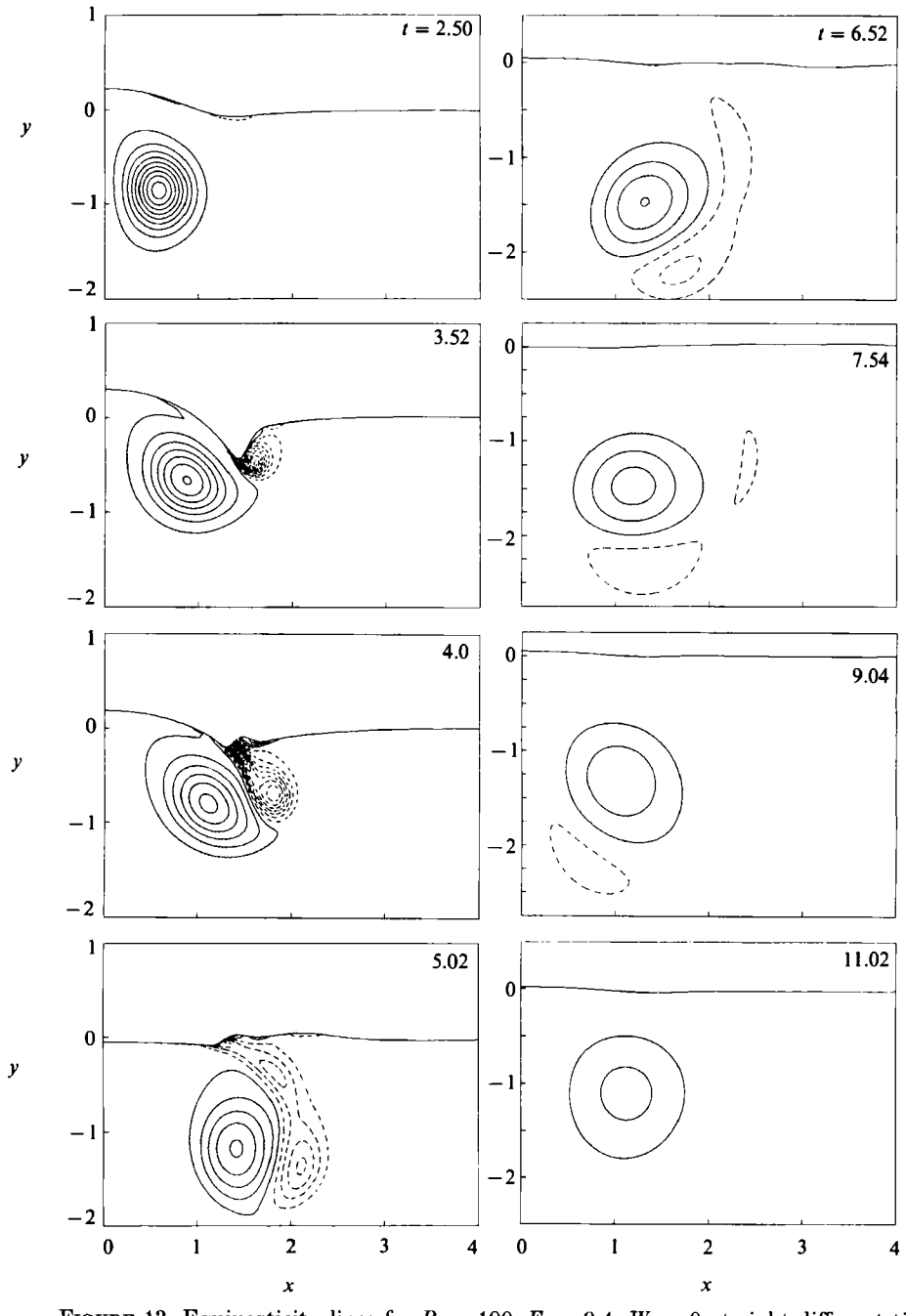

FIGURE 13. Equivorticity lines for $Re = 100$, $Fr = 0.4$, $We = 0$ at eight different times. The ω-contours are ..., -3, -1, $+1$, $+3$, ...

supported by flows with surface tension which tends to flatten a disturbed surface (figure 15).

As in the cases for $Fr = 0.2$ and 0.8, the maximum absolute vorticity $|\omega_{\text{extremum}}|$ of the primary vortex decays for $Fr = 0.4$ according to (16), which means that the centre part of the vortex is not influenced by the changing flow field around it (figure

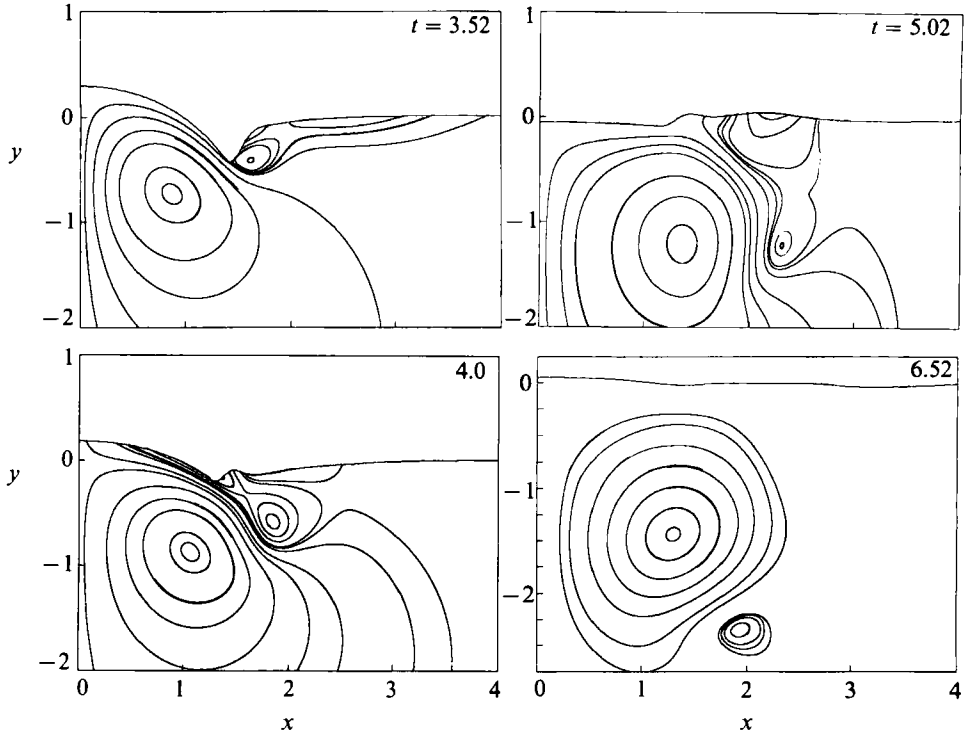

FIGURE 14. Streamlines for $Re = 100$, $Fr = 0.4$, $We = 0$ at four different times.

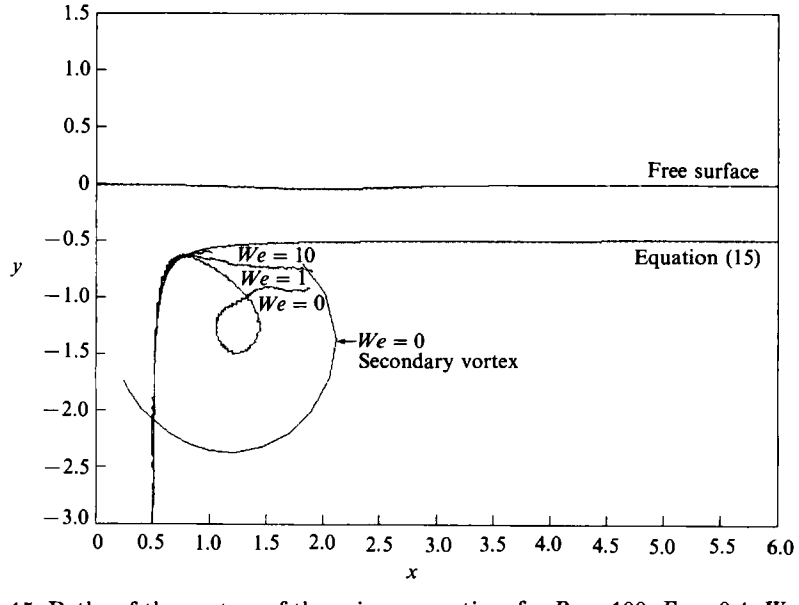

FIGURE 15. Paths of the centres of the primary vortices for $Re = 100$, $Fr = 0.4$, $We = 0$, 1, and 10 and of the secondary vortex for $Re = 100$, $Fr = 0.4$, $We = 0$. For comparison, Lamb's potential-flow solution for a flat surface is included. The free surface is plotted for the final time $t = 17.02$.

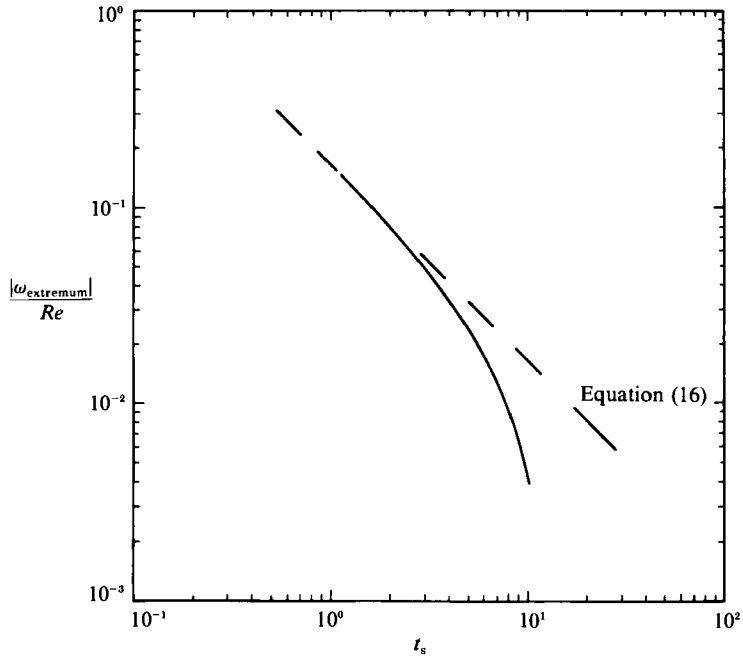

FIGURE 16. Decay of secondary vortex of figure 13 with time.

7). Beyond $t = 6$ the vortex decays faster. The secondary vortex decays also according to (16), i.e. proportional to the inverse of time t_s, in which t_s is the time extrapolated backwards to an artificial beginning as a potential vortex (figure 16). In this special case, t_s is $t-2.8786$. Then the vortex decays faster, as do the primary vortices in figure 7. A curve similar to that of figure 16 (equation (16)) with faster decay at later time was also found by Lugt & Haussling (1974) for vortices shed from an elliptic cylinder, vortices which were not introduced at $t = 0$ according to (11) but were generated by the evolving flow field past the body.

In order to study the influence of surface tension, the vorticity and flow fields for $Fr = 0.4$, $We = 0$ and $We = 1$ are compared (figures 13, 14, 17, and 18). The scar at $t = 3.52$ in figure 17 is less pronounced owing to surface tension, but enough surface vorticity is produced to form a weak counter-rotating secondary vortex. There is high-speed flow close to and in a direction tangential to the free surface scar, indicated by a crowding of streamlines (figure 18, $t = 3.52$). The primary vortex moves almost parallel to the surface and pushes in front of it the secondary vortex (figure 17, $t = 5.02$) whose presence causes only a slight deviation of the circular streamline pattern of the primary vortex (figure 18, $t = 5.02$).

The flow for $Fr = 0.4$, $We = 10$ is almost the same as that for $Fr = 0.2$, $We = 10$ (figure 19). No surface vorticity worth mentioning is generated.

For the above comparison, it is helpful to plot the surface vorticity and tangential surface velocity at various times (figures 20 and 21). The smoothing effect of surface tension and the diminished vorticity production are clearly visible.

It may be noticed, when comparing figure 20 with figure 7, that the surface vorticity can be larger at times than the extremal vorticity of the original primary vortex which caused the surface disturbance. This is an interesting situation because it means that, in principle, secondary vortices can be created that are stronger than the primary vortex.

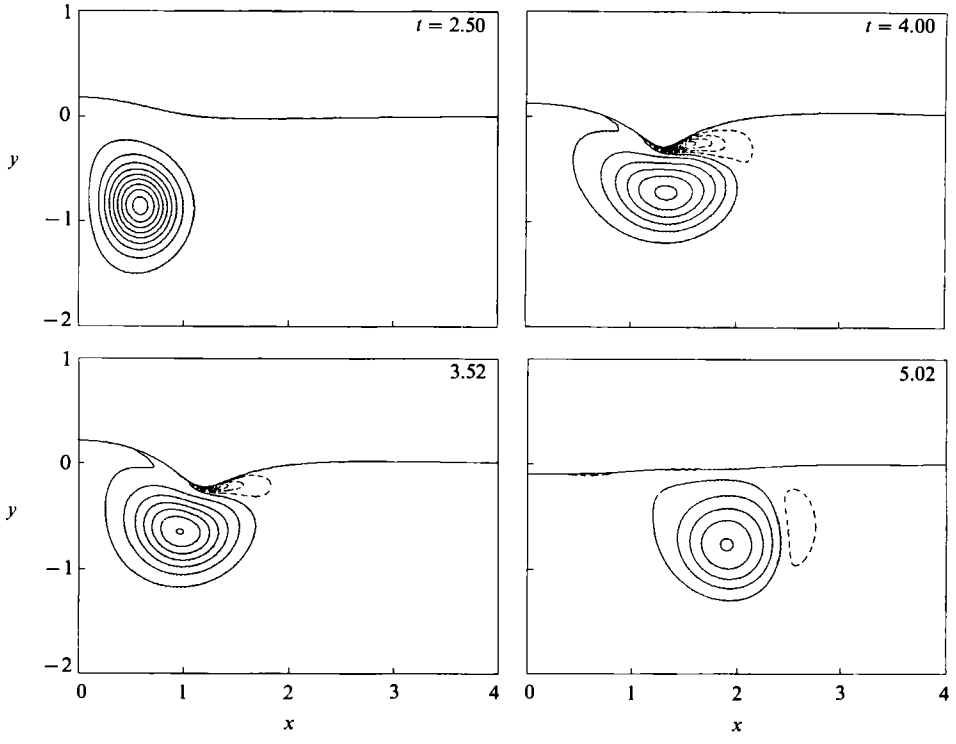

FIGURE 17. Equivorticity lines for $Re = 100$, $Fr = 0.4$, $We = 1$ at four different times. The ω-contours are ..., -3, -1, $+1$, $+3$, ...

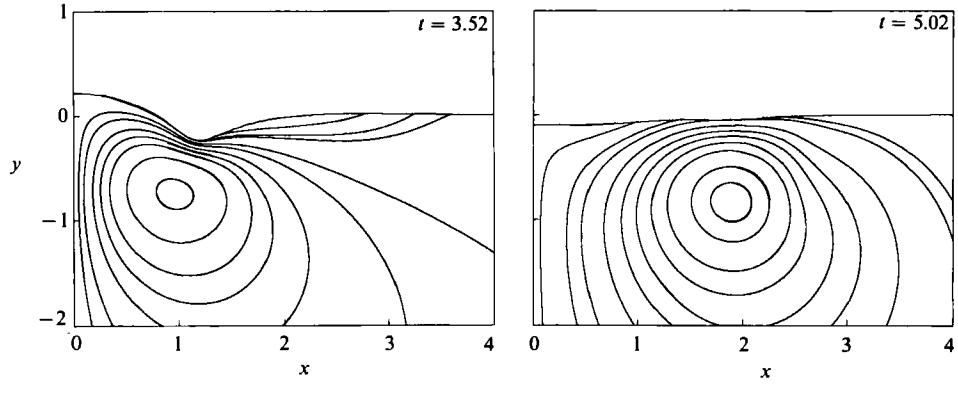

FIGURE 18. Streamlines for $Re = 100$, $Fr = 0.4$, $We = 1$ at two different times.

Figure 21 shows that the tangential surface velocity $(v_t)_s$ is considerably larger and always positive, i.e. in the direction of increasing x along the free surface, for the surface tension case $We = 1$ compared to that of the non-surface tension case $We = 0$. In the latter case, $(v_t)_s$ becomes negative in the scar (figure 13, $t = 4$), i.e. there is a reversal of the flow direction along the free surface. Despite the larger tangential velocity of $We = 1$, the surface vorticity is smaller than that for $We = 0$ (figure 20) owing to the greatly diminished surface curvature. Because of this larger surface

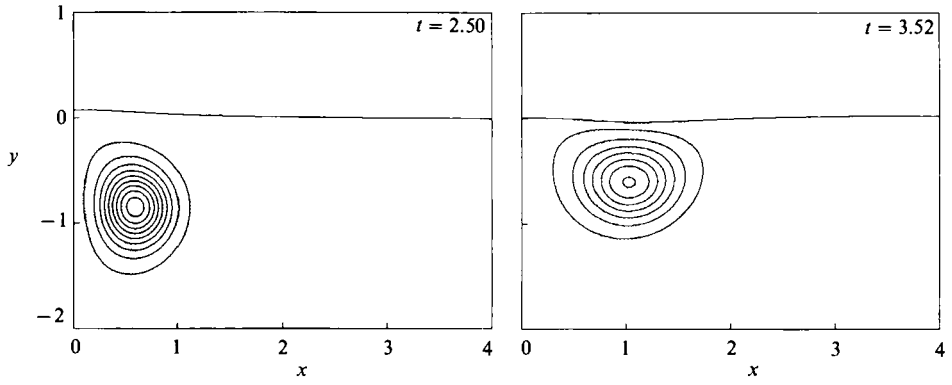

FIGURE 19. Equivorticity lines for $Re = 100$, $Fr = 0.4$, $We = 10$ at two different times. The ω-contours are ..., -3, -1.

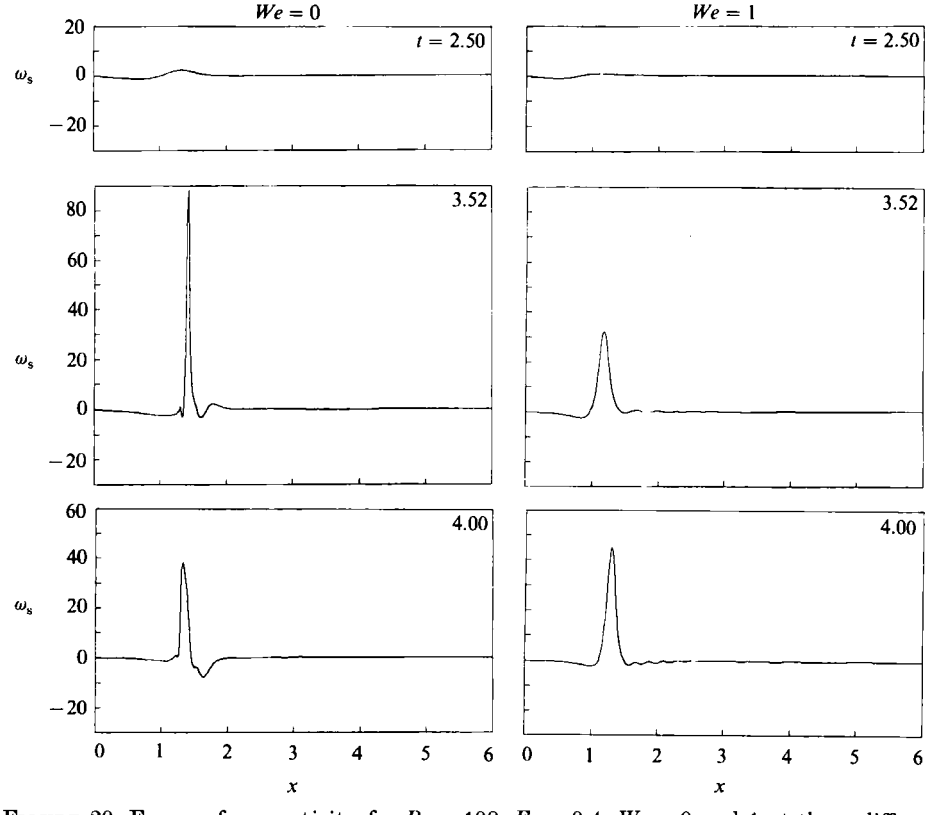

FIGURE 20. Free-surface vorticity for $Re = 100$, $Fr = 0.4$, $We = 0$ and 1 at three different times.

velocity, the surface tension case $We = 1$ required the use of a smaller physical time step in the numerical scheme than that for $We = 0$.

Finally, the flow fields are discussed for two Reynolds numbers smaller than 100, that is, for $Re = 50$ and 10. The equivorticity lines with surface elevations for $Re = 50$, $Fr = 1.125$ are displayed in figure 22. As in the case of $Re = 100$, $Fr = 0.8$, the computation is terminated at $t = 4.06$ for numerical reasons. At the high Froude number of 1.125 the surface elevations and trajectories of the vortex centre in figure

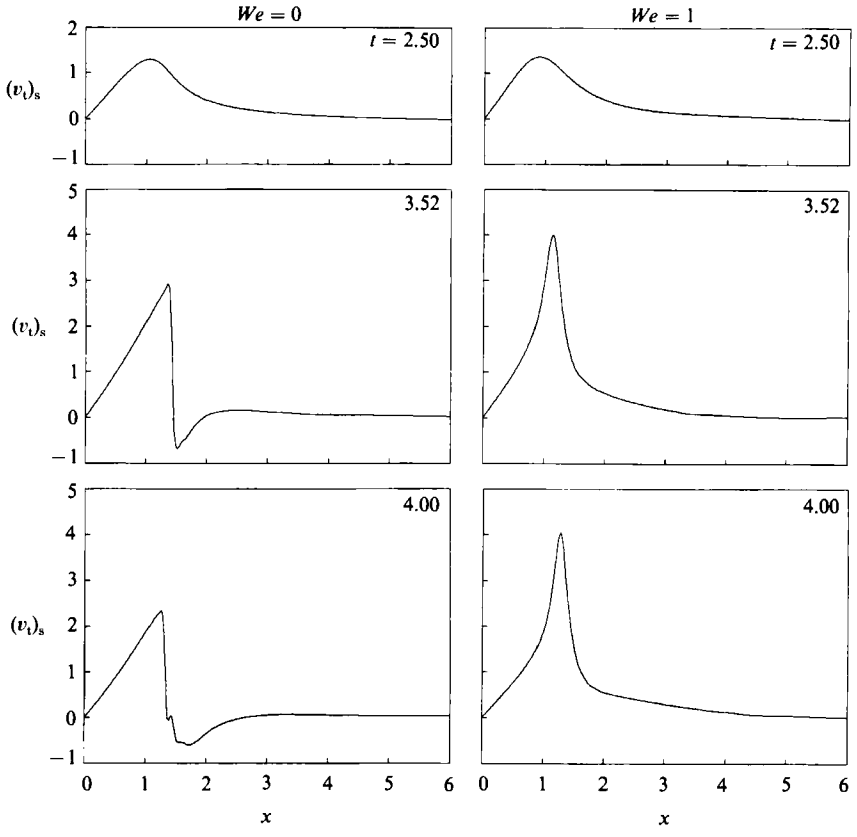

FIGURE 21. Tangential velocity at the free surface for $Re = 100$, $Fr = 0.4$, $We = 0$ and 1 at three different times.

23 (*a*) are apparently not sensitive to changes of the Reynolds number, at least from $Re = 50$ and higher, as a comparison of the $Re = 50$ case with that for $Re = 100$ and the inviscid-flow case reveals (figure 22 may be compared with figures 5(*a*), 5(*c*), and 5(*e*) of Sarpkaya *et al.* (1988). The dimensionless time T in their work is related to the time herein t by $T = t-3$. The same comparison can be made with the work of Marcus (1988) and Telste (1989). The results for $Re = 10$, however, presented below, indicate a different situation: the free surface barely rises above the undisturbed level owing to viscous effects.

For $Re = 50$, $Fr = 0.356$, the influence of the Reynolds number can be felt when the shape of the free surface and the vortex path are compared with those of $Re = 100$, $Fr = 0.4$. The scar in figure 24 ($t = 3.52$) is less pronounced than the scar in figure 13 that results in less vorticity production. Although a secondary vortex develops, it is not whirled around the primary vortex but pushed ahead of it parallel to the free surface. The path of the primary vortex does not form a loop as in the case of $Re = 100$ but shows only weak rebounding in figure 23 (*b*). Figure 24 is similar to figure 17 for $Re = 100$, $Fr = 0.4$, $We = 1$ in which surface tension flattens the scar and diminishes the vorticity production.

The free surface undergoes damped oscillation during the whole encounter. Its maximum elevation at the centreline differs only slightly from those for $Re = 100$ and the inviscid case (Telste 1989). For the slightly higher Froude number of 0.5, the

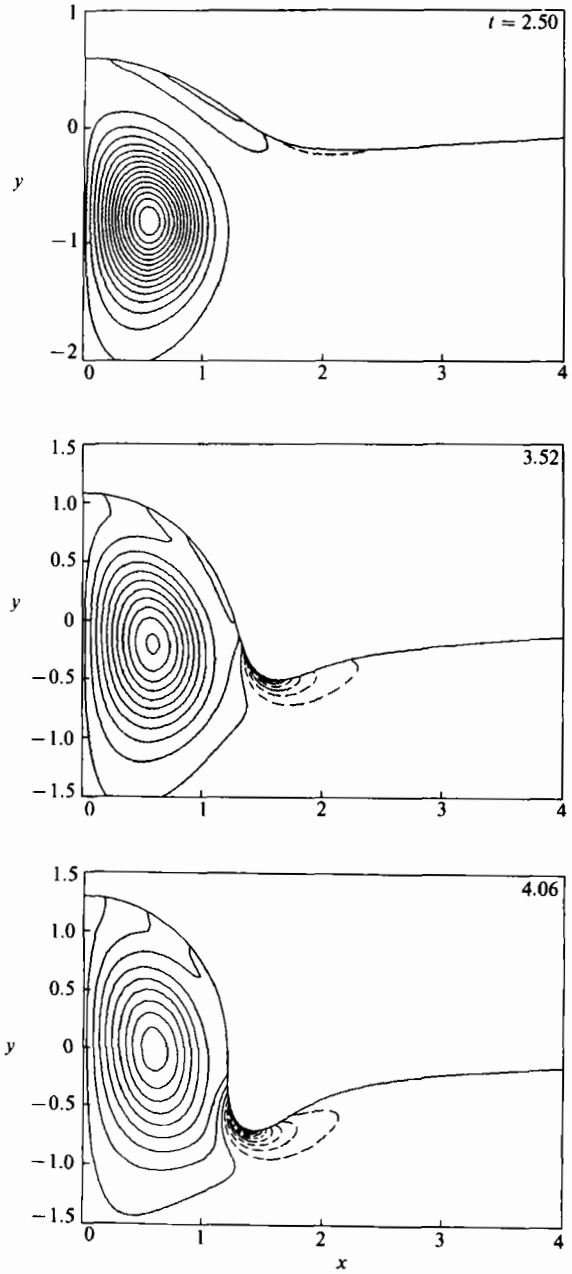

FIGURE 22. Equivorticity lines for $Re = 50$, $Fr = 1.125$, $We = 0$ at three different times. The ω-contours are ..., -1.5, -0.9, -0.3, $+0.3$, ...

numerical results by Sarpkaya *et al.* (1988) showed qualitative agreement with experiments.

In the case of $Re = 10, Fr = 1.125$ diffusion dominates convection so much that the maximum elevation $y = 0.307$ at $t = 4.0$ is small compared to all previous cases at this high Froude number without surface tension. The free surface returns, after the

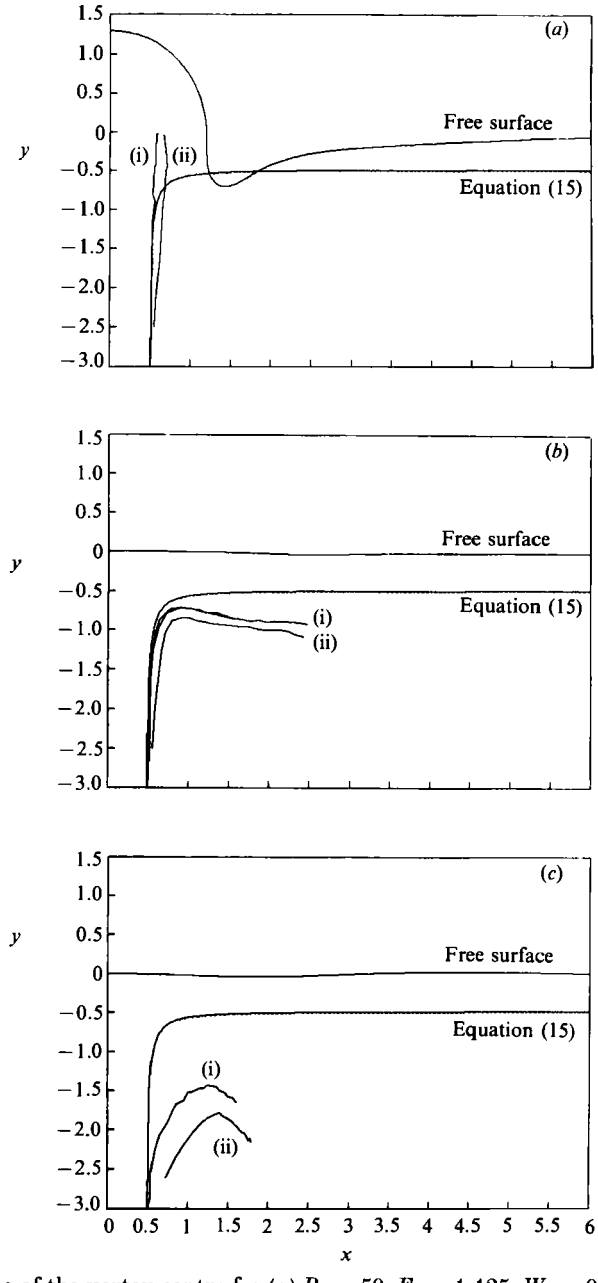

FIGURE 23. Paths of the vortex centre for (*a*) $Re = 50, Fr = 1.125, We = 0$, (*b*) $Re = 50, Fr = 0.356, We = 0$, and (*c*) $Re = 10, Fr = 1.125, We = 0$. The curves (i) represent the paths of extremal vorticity and the curves (ii) the centres of nested streamlines. The free surfaces are plotted for the final times (*a*) $t = 4.06$, (*b*) $t = 9.52$, and (c) $t = 9.04$.

maximum elevation has been reached, without oscillation to the state at rest. Figure 25 shows equivorticity lines at $t = 4.48$ and $t = 9.04$.

The path of the vortex centre is plotted in figure 23(*c*). Rebounding is much stronger than in the other cases with slightly disturbed free surfaces as, for instance, in the cases of $Re = 50$, $Fr = 0.356$ and $Re = 100$, $Fr = 0.2$. This comparison clearly

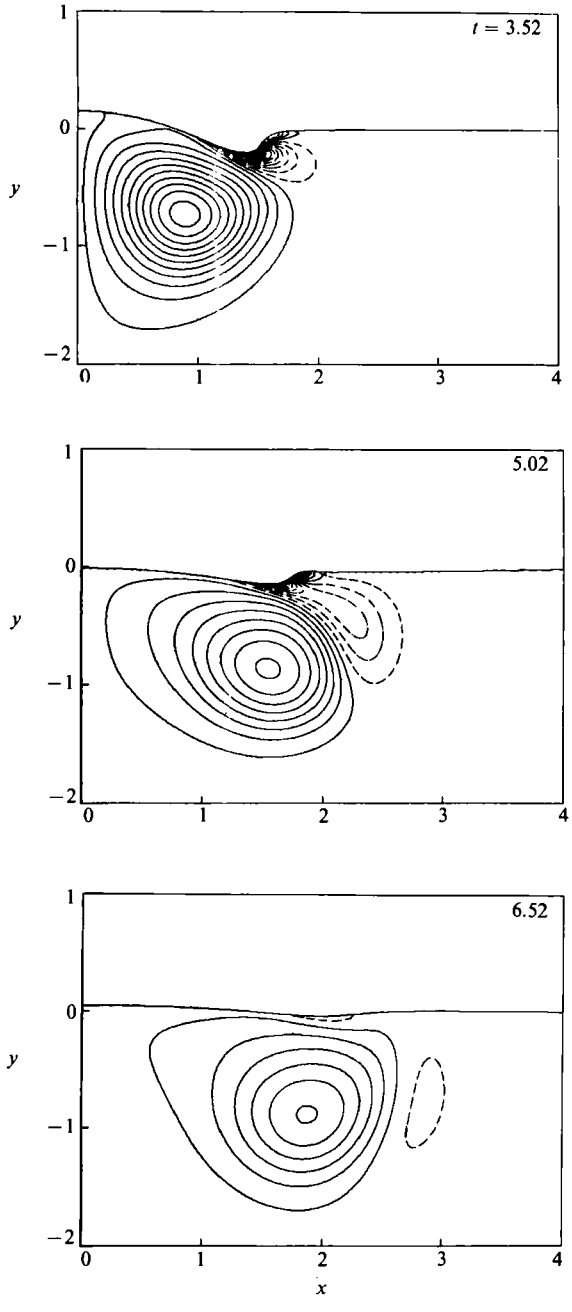

FIGURE 24. Equivorticity lines for $Re = 50$, $Fr = 0.356$, $We = 0$ at three different times. The ω-contours are ..., -1.5, -0.9, -0.3, $+0.3$, ... The patterns for $t = 5.02$ were computed with a finer grid and do not show yet a pinched-off secondary vortex, while the patterns computed with the original grid do.

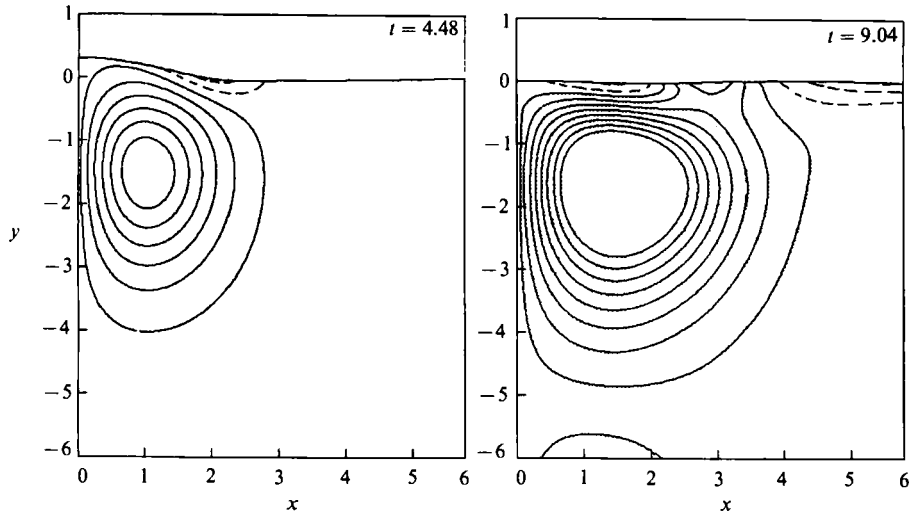

FIGURE 25. Equivorticity lines for $Re = 10$, $Fr = 1.125$, $We = 0$ at two different times. At $t = 4.48$, the ω-contours are ..., -0.25, -0.15, -0.05, $+0.05$, ... At $t = 9.04$, the ω-contours are -0.15, -0.13, ...

provides evidence that rebounding at a flat surface diminishes with increasing Reynolds number, that is, with decreasing diffusion. This confirms recent numerical results by Orlandi (1990).

Additional details on the flow fields for $Re = 10$ and 50 can be found in I.

This work was supported jointly by the DTRC Independent Research Program and by the Office of Naval Research, Fluid Dynamics Program, under Dr E. P. Rood.

REFERENCES

BARKER, S. J. & CROW, S. C. 1977 The motion of two-dimensional vortex pairs in a ground effect. *J. Fluid Mech.* **82**, 659–671.

BATCHELOR, G. K. 1967 *An Introduction to Fluid Dynamics*, p. 366. Cambridge University Press.

BERNAL, L. P., HIRSA, A., KWON, J. T. & WILLMARTH, W. W. 1989 On the interaction of vortex rings and pairs with a free surface for varying amounts of surface active agent. *Phys. Fluids* A **1**, 2001–2004.

COUDER, Y. & BASDEVANT, C. 1986 Experimental and numerical study of vortex couples in two-dimensional flows. *J. Fluid Mech.* **173**, 225–251.

DAGAN, A. 1989 Pseudo-spectral and asymptotic sensitivity investigation of counter-rotating vortices. *Computers & Fluids* **17**, 509–525.

FISH, S. 1990 Ambient free surface wave modification by a submerged vortex pair. *David Taylor Research Center Rep. DTRC*-90/004.

FLORYAN, J. M. & RASMUSSEN, H. 1989 Numerical methods for viscous flows with moving boundaries. *Appl. Mech. Rev.* **42**, 323–341.

HARVEY, J. K. & PERRY, F. J. 1971 Flowfield produced by trailing vortices in the vicinity of the ground. *AIAA J.* **9**, 1659–1660.

KOCHIN, N. E., KIBEL, I. A. & ROZE, N. V. 1964 *Theoretical Hydromechanics*. Wiley.

LAMB, H. 1932 *Hydrodynamics*. Dover.

LUGT, H. J. 1983 *Vortex Flow in Nature and Technology*. Wiley-Interscience.

LUGT, H. J. & HAUSSLING, H. J. 1974 Laminar flow past an abruptly accelerated elliptic cylinder at 45° incidence. *J. Fluid Mech.* **65**, 711–734.

MARCUS, D. L. 1988 The interaction between a pair of counter-rotating vortices and a free boundary. Ph.D. thesis, University of California at Berkeley.

NGUYEN DUC, J. & SOMMERIA, J. 1988 Experimental characterization of steady two-dimensional vortex couples. *J. Fluid Mech.* **192**, 175–192.

NOVIKOV, Y. A. 1981 Generation of surface waves by discrete vortices. *Izv. Akad. Nauk. SSSR Atmos. Ocean. Phys.* **92**, 497–503.

OHRING, S. & LUGT, H. J. 1989 Two counter-rotating vortices approaching a free surface in a viscous fluid. *David Taylor Research Center Rep. DTRC*-89/013 (referred to herein as I).

ORLANDI, P. 1990 Vortex dipole rebound from a wall. *Phys. Fluids* A **2**, 1429–1436.

PEACE, A. J. & RILEY, N. 1983 A viscous vortex pair in ground effect. *J. Fluid Mech.* **129**, 409–426.

SAFFMAN, P. G. 1979 The approach of a vortex pair to a plane surface in inviscid fluid. *J. Fluid Mech.* **92**, 497–503.

SALVESEN, N. & KERCZEK, C. VON 1976 Comparison of numerical and perturbation solutions of two-dimensional nonlinear water-wave problems. *J. Ship Res.* **20**, 160–170.

SARPKAYA, T. 1986 Trailing-vortex wakes on the free surface. In *Proc. 16th Symp. on Naval Hydrodynamics, Berkeley*, pp. 38–50.

SARPKAYA, T., ELNITSKY, J. & LEEKER, R. E. 1988 Wake of a vortex pair on the free surface. In *Proc. 17th Symp. on Naval Hydrodynamics*, pp. 47–54. Washington: Naval Studies Board.

SARPKAYA, T. & HENDERSON, D. O. 1984 Surface disturbances due to trailing vortices. *Naval Postgraduate School, Monterey, California, Rep. NPS*-69-84-004.

SARPKAYA, T. & SUTHON, P. B. 1990 Scarred and striated signature of a vortex pair on the free surface. *Proc. 18th Symp. on Naval Hydrodynamics.* National Academy Press (to appear).

TELSTE, J. G. 1989 Potential flow about two counter-rotating vortices approaching a free surface. *J. Fluid Mech.* **201**, 259–278.

THOMPSON, J. F. & SHANKS, S. P. 1977 Numerical solution of the Navier–Stokes equations for 2d surface hydrofoils. *Mississippi State University Rep. MSSU-EIRS-ASE*-77-4.

TRYGGVASON, G. 1988 Deformation of a free surface as a result of vortical flows. *Phys. Fluids* **31**, 955–957.

WALKER, J. D. A., SMITH, C. R., CERRA, A. W. & DOLIGALSKI, T. L. 1987 The impact of a vortex ring on a wall. *J. Fluid Mech.* **181**, 99–140.

WEHAUSEN, J. V. & LAITONE, E. V. 1960 Surface waves. In *Handbuch der Physik*, Vol. IX, pp. 446–778. Springer.

WILLMARTH, W. W., TRYGGVASON, G., HIRSA, A. & YU, D. 1989 Vortex pair generation and interaction with a free surface. *Phys. Fluids* A **1**, 170–172.

YEUNG, R. W. 1982 Numerical methods in free-surface flows. *Ann. Rev. Fluid Mech.* **14**, 395–442.